




## Intralayer strain tuned interlayer magnetism in bilayer CrSBr

Nanshu Liu <sup>1,2</sup> Cong Wang,<sup>1,2</sup> Yaqiong Zhang,<sup>1,2,3</sup> Fei Pang <sup>1,2</sup> Zhihai Cheng,<sup>1,2</sup> Yanning Zhang,<sup>4</sup> and Wei Ji <sup>1,2,4,\*</sup>

<sup>1</sup>Beijing Key Laboratory of Optoelectronic Functional Materials & Micro-Nano Devices, Department of Physics, Renmin University of China, Beijing 100872, China

<sup>2</sup>Key Laboratory of Quantum State Construction and Manipulation (Ministry of Education), Renmin University of China, Beijing 100872, China

<sup>3</sup>Physics Teaching and Research Office, Shanxi Institute of Science and Technology, Jincheng 048011, China

<sup>4</sup>Institute of Fundamental and Frontier Sciences, University of Electronic Science and Technology of China, Chengdu 610054, China



(Received 29 January 2024; accepted 31 May 2024; published 17 June 2024)

Interlayer magnetism was tuned by many interlayer means, e.g., stacking, distance, and external fields in two-dimensional (2D) magnets. As an exception, the interlayer magnetism of CrSBr few layers was, however, experimentally changed by applied intralayer strains [Nat. Nanotechnol. **17**, 256 (2022)], the mechanism of which is yet to be unveiled. Here, we uncovered its mechanism by investigating in-plane strained bilayer CrSBr using density functional theory calculations. Under in-plane tensile strain, wavefunction overlaps are strengthened for Br  $p$  electrons within each CrSBr layer, which delocalizes intralayer electrons and, as a consequence, promotes interlayer electron hopping. A negative interlayer Poisson's ratio also enlarges interlayer spacing for bilayer CrSBr, which reduces the interlayer Pauli repulsion. This joint effect, further verified by examining interlayer sliding and interfacial element substitution, leads to an interlayer antiferromagnetic to ferromagnetic transition, consistent with the previous experimental observation. This mechanism enables a route to tune interlayer magnetism by modifying intralayer electron localization in 2D magnets.

DOI: [10.1103/PhysRevB.109.214422](https://doi.org/10.1103/PhysRevB.109.214422)

### I. INTRODUCTION

Two-dimensional (2D) van der Waals (vdW) materials host strongly anisotropic interatomic interactions that covalent bonding governs their in-plane interactions but noncovalent bonding dominates out-of-plane ones. Unlike the  $r^{-6}$  relation revealed in gas phase molecules, the enhanced dispersion attraction among 2D layers [1] results in substantial wavefunction overlaps between out-of-plane electron orbitals of two adjacent layers [2]. Breakdown of the overlaps usually requires hundreds of meV [3], which is an order of magnitude smaller than that of typical covalent bonds. Such small energy cost enables many feasible strategies for interlayer tuning [4,5] of wavefunction overlaps that significantly affect interlayer electronic [6], optical [7], and recently magnetic [8,9] properties of 2D materials. After the first exfoliation of ferromagnetic (FM) monolayer (ML) [10,11], interlayer magnetism of 2D magnetic materials was demonstrated to be tunable by interlayer (out-of-plane) means, such as distance [12], stacking [13,14], electrical field [15,16], proximity effects from substrates [17], charge doping [18], intercalation [19], or among the others [20,21]. All these tuning strategies were applied, primarily, in the out-of-plane direction. Intralayer [22–24] and interlayer [25] strains were used to modulate the intralayer magnetism of 2D magnets, however, an exceptional case lies in tuning the interlayer magnetism using in-plane strain in a CrSBr thin film [26].

Bulk CrSBr is a vdW material exhibiting the A-type antiferromagnetism (AFM) below its Néel temperature ( $T_N$ ).

Each layer of it is in an FM order, but couples to adjacent layers in the AFM configuration. The critical temperature ( $T_N \sim 132$  K) is preserved down to the CrSBr bilayer (BL) [27]. A reversible interlayer AFM-to-FM phase transition was experimentally evidenced under an applied in-plane uniaxial strain ( $\varepsilon$ ) along the shorter edge [the  $x$  direction; see Fig. 1(a)] of a CrSBr thin film [26]. This transition is exceptional and the reasoning is still unclear so far as to why such interlayer magnetism could be reversibly changed by in-plane strains although the theoretical calculations jointly reported in Ref. [26] indicated that the in-plane strain does modify the interlayer magnetic exchange energies.

In this work, we explored the roles of uniaxial in-plane strain along the shorter edge (the  $x$  direction) in tuning the interlayer magnetic coupling of bilayer CrSBr using density functional theory (DFT) calculations. We first reproduced the experimentally observed interlayer AFM to FM transition, which is theoretically predicted to be under an in-plane uniaxial  $x$  strain of 3.2% or larger in the bilayer CrSBr model. Such a transition originates from tension induced delocalization of interlayer shared valence electrons, the mechanism of which was unveiled by comparing the strength of interlayer electronic hybridization and kinetic energy, and by examining the spin density, spin-resolved differential charge density and squares of wavefunction norms. Finally, we also discussed the roles of vertical and lateral sliding, or element substitution to verify the mechanism.

### II. COMPUTATIONAL DETAILS

Our DFT calculations were performed using the generalized gradient approximation parametrized by Perdew, Burke,

\*Contact author: wji@ruc.edu.cn

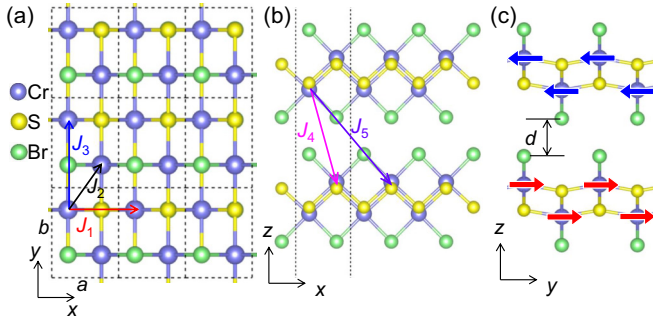


FIG. 1. Atomic and magnetic structures of bilayer CrSBr. (a), (b) Top and side views of bilayer CrSBr. Blue, yellow, and green balls represent Cr, S, and Br atoms, respectively. Red, black, and blue arrows in (a) denote three intralayer spin-exchange parameters  $J_1$ ,  $J_2$ , and  $J_3$  between Cr sites. Pink and purple arrows in (b) are two interlayer spin-exchange parameters  $J_4$  and  $J_5$ . The black dashed lines are the lattice of CrSBr. (c) Magnetic moments of Cr atoms in bilayer CrSBr. Red and blue arrows represent the magnetic moments of Cr atoms along the  $+y$  and  $-y$  directions, respectively. Interlayer spacing is denoted by  $d$ .

and Ernzerhof (GGA-PBE) for the exchange-correlation potential [28], the projected augmented wave (PAW) method [29], and a plane-wave basis set as implemented in the Vienna *ab initio* simulation package (VASP). The kinetic energy cutoff for the plane waves was set to 700 eV for geometric optimization and 600 eV for electronic structure calculations. A DFT+ $U$  method was used in all calculations, where  $U = 2.0$  eV and  $J = 1.0$  eV. This choice of  $U$  and  $J$  accurately reproduces the interlayer AFM ground state for the strain-free CrSBr bilayer (Fig. S1 of the Supplemental Material [30]), and comparable values have been used in the literature for modeling bulk CrSBr [31]. A uniform Monkhorst-Pack  $k$ -mesh of  $19 \times 15 \times 1$  was adopted for sampling the first Brillouin zone. A vacuum layer of 20 Å was included to eliminate interactions among image slabs. The dispersion correction was applied at the van der Waals density functional (vdW-DF) level, with the optB86b functional for the exchange potential, which has been shown to accurately describe structure-related properties of many layered materials [6,32,33]. For energy comparisons, we used the PBE functional and considered spin-orbit coupling (SOC) based on the atomic structures revealed by vdW-DF. All atoms and lattice parameters were allowed to relax until the residual force per atom was less than 0.01 eV/Å. Uniaxial strains along the  $x$  direction were applied by varying the lattice constant in the  $x$  direction to given values while allowing the other direction to relax. The volumes and shapes of unstrained bilayer CrSBr and those under uniaxial strains along the  $x$  or  $y$  directions were optimized, while the volumes and shapes for bilayer CrSBr under biaxial and epitaxial strains were kept constant. We sliced the interlayer differential charge densities (DCDs) parallel to the  $x$ - $z$  plane, crossing the middle of lattice  $b$  [Fig. 1(a)], to display the 2D maps. The intralayer portion was omitted for clarity. Spatial variations of interlayer DCDs across the vdW gap (the Cr atoms) were obtained by extracting line profiles of averaged charge densities in the middle  $x$ - $y$  plane and the vdW gap (in the plane containing the Cr atoms). A linear

interpolation of discrete epitaxial strains was used to provide a more complete view of the magnetic phase boundary. Detailed computational methods can be found in the Supplemental Material (SM) [30].

### III. RESULTS AND DISCUSSIONS

The fully optimized lattice parameters of bilayer CrSBr are  $a = 3.52$  Å and  $b = 4.74$  Å. Bilayer CrSBr shows an intralayer FM and interlayer AFM ground state, with the intralayer first, second, and third nearest-neighbor exchange parameters  $J_1 = 1.57$  meV,  $J_2 = 2.29$  meV and  $J_3 = 2.78$  meV [Fig. 1(a); positive values represent the FM coupling], and interlayer  $J_4 = -0.01$  meV and  $J_5 = -0.20$  meV [Fig. 1(b)]. The magnetic moments of Cr atoms are parallel to the  $b$  ( $y$ ) direction in each layer [Fig. 1(c)] exhibiting a magnetic anisotropic energy (MAE) of 0.10 meV/Cr, consistent with the experimentally observed [26] and theoretically predicted [34,35] direction of magnetic moments.

In order to theoretically reproduce the experimentally observed AFM-to-FM transition, we applied a uniaxial strain on the CrSBr bilayer along the  $x$  direction (the shorter edge in the experiment [26]). Figure 2(a) shows that lattice constant  $b$  (in red) decreases from 4.75 to 4.72 Å and the interlayer spacing ( $d$ , in blue) increases from 2.34 to 2.43 Å when the in-plane  $x$  strain  $\varepsilon_x$  changes from  $-2.0\%$  to  $4.2\%$ . Here, we define an interlayer Poisson's ratio  $\nu_{\text{inter}} = -\frac{\Delta d/d}{\varepsilon_x}$  where  $\Delta d/d$  is the change of interlayer spacing  $d$  under an in-plane strain  $\varepsilon_x$  [22], which was derived to be  $-0.79$  for the CrSBr bilayer, exhibiting an abnormal negative value. An abrupt shrink of  $d$  was found at  $\varepsilon_x = 3.0\%$  [blue solid dot in Fig. 2(a)], followed by a crossover of interlayer AFM to FM at  $\varepsilon_x = 3.2\%$  [Fig. 2(b)]. A similar transition occurs under in-plane epitaxial tensile strains along the  $x$  and  $y$  directions [red region in Fig. 2(c)], as well as a biaxial tensile strain larger than 2.5% (Fig. S3f of the SM [30]). However, the interlayer AFM state remains robust under uniaxial  $y$  strains (Fig. S3c).

Given the experimental observation reproduced, we next plotted the spin densities of the bilayers for the interlayer FM states under  $\varepsilon_x = 4.2\%$  [Fig. 2(d)] and  $0.0\%$  [Fig. 2(e)] in side views, which are two representative bilayers favoring the interlayer FM and AFM states, respectively. The spin densities around the interlayer Br atoms [marked by blue dashed boxes in Fig. 2(e)] of the  $\varepsilon_x = 4.2\%$  case [Fig. 2(d)] are slightly smaller than those for  $\varepsilon_x = 0.0\%$  [Fig. 2(e)]. The decreased spin density at the vdW gap for  $\varepsilon_x = 4.2\%$  is further reflected by its variations [orange line in Fig. 2(f)] across the two interfacial Br atoms [Br1 and Br2 in Fig. 2(d)]. A likely reason for this downsized contour lies in delocalization of electron around the Br atoms under  $\varepsilon_x = 4.2\%$ , which was supported by the plotted interlayer DCDs. Figures 2(g)–2(j) show slabs, parallel to the  $x$ - $z$  plane, of the DCDs for the majority spin channel under  $\varepsilon_x$  varying from  $-2.0$  [Fig. 2(g)] to  $4.2\%$  [Fig. 2(j)]. For compressed [Fig. 2(g)] or strain-free [Fig. 2(h)] CrSBr bilayers, accumulated charge densities (red regions) are localized between the interlayer Br atoms, while they gradually become more delocalized under larger tensile strains, e.g.,  $\varepsilon_x = 3.2\%$  [Fig. 2(i)], and ultimately form a one-dimensional (1D) continuous distribution in the vdW gap of the bilayer for

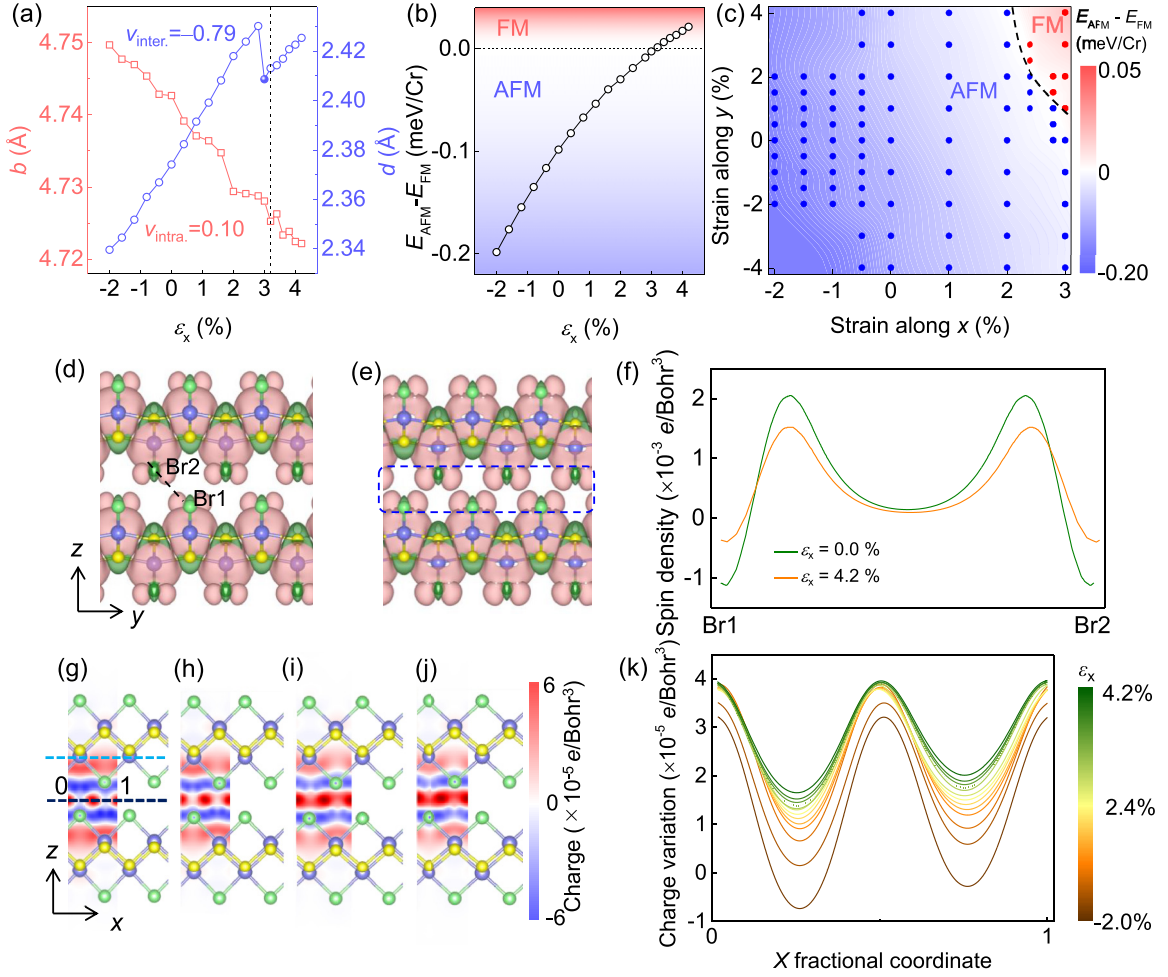


FIG. 2. Structural and interlayer magnetic properties of bilayer CrSBr under a uniaxial strain along the  $x$  direction ( $\epsilon_x$ ), including (a) lattice parameter  $b$  (red squares) and interlayer spacing  $d$  (blue dots). Inter- and intralayer Poisson ratios are labeled by  $\nu_{\text{inter}}$  and  $\nu_{\text{intra}}$ ; (b) energy difference between the interlayer AFM ( $E_{\text{AFM}}$ ) and FM ( $E_{\text{FM}}$ ) states as a function of  $\epsilon_x$ . (c) Energy difference between interlayer AFM and FM couplings under epitaxial strains. The black dashed line labels the interlayer AFM and FM boundary. Spin densities for (d)  $\epsilon_x = 4.2\%$  and (e)  $\epsilon_x = 0.0\%$  with interlayer FM coupling. The majority and minority spin channels were presented by red and green isosurfaces, respectively, with a value of  $3 \times 10^{-4} e/\text{Bohr}^3$ . The interlayer coupling region is outlined by a blue dashed box. (f) Spin density variations along the black dashed line between the two Br atoms [Br1 and Br2 in panel (d)] with interlayer FM coupling. The spin densities around the interlayer Br atoms of  $\epsilon_x = 4.2\%$  are slightly smaller than those for  $\epsilon_x = 0.0\%$ . (g)–(j) 2D maps, parallel to the  $x$ - $z$  plane crossing the middle of lattice  $b$  [Fig. 1(a)], of interlayer differential charge densities for bilayer CrSBr with  $\epsilon_x = -2.0\%$ ,  $0.0\%$ ,  $3.2\%$ , and  $4.2\%$ , respectively. The red and blue contours are electron accumulation and depletion, respectively. (k) Spatial variation of averaged charge densities in the  $x$ - $y$  plane along the black dashed line in (g) for different strains. The interlayer AFM to FM transition strain of  $\epsilon_x = 3.2\%$  is labeled by a dashed line.

$\epsilon_x = 4.2\%$  [Fig. 2(j)]. This trend is quantitatively illustrated in line profiles [Fig. 2(k)] of the averaged charge densities in the  $x$ - $y$  plane across the middle of the vdW gap [black dashed line denoted in Fig. 2(g)], in which the larger the tensile strain, the smoother the averaged charge density. While there are some charge accumulations (Fig. S4) around the Cr atoms [labeled by the blue dashed line in Fig. 2(i)], these charges are localized and, most likely, have a minor impact on the interlayer magnetic coupling. Such strain induced delocalization was also supported by plotting a line profile of the electron localization function (ELF) across two nearest-neighboring Br atoms in the same plane (see the white dashed line in Fig. S5a) where the ELF for  $\epsilon_x = 4.2\%$  is always smaller than that for  $\epsilon_x = 0.0\%$  in the interatomic region (Fig. S5c). In short, uniaxial tensile  $x$  strains lead to more delocalized interlayer

sharing electrons, which could lower the kinetic energy for these electrons exchanging across the vdW gap and is, most likely, relevant to the interlayer AFM to FM transition.

The real-space visualized electron delocalization is also reflected in the energy and/or  $k$  space. Figures 3(a) and 3(b) show electronic band structures of the strain-free CrSBr mono- and bilayers. There are two bands [labeled V1 (red) and V2 (blue) in Fig. 3(a)] near the VBM of the monolayer, exhibiting a significant anisotropy along the  $G$ - $X$  and  $G$ - $Y$  directions. The V1 and V2 bands are comprised of Br  $p_y$  and Cr  $d_{yz}$  orbitals, as illustrated in Figs. 3(c) and 3(d), consistent with our previous calculation results [36] and the literature [35]. In bilayer CrSBr, the two V1 bands from both layers hybridize into a pair of interlayer antibonding [V1-AB, violet in Fig. 3(b)] and bonding [V1-B, red in Fig. 3(b)] bands through

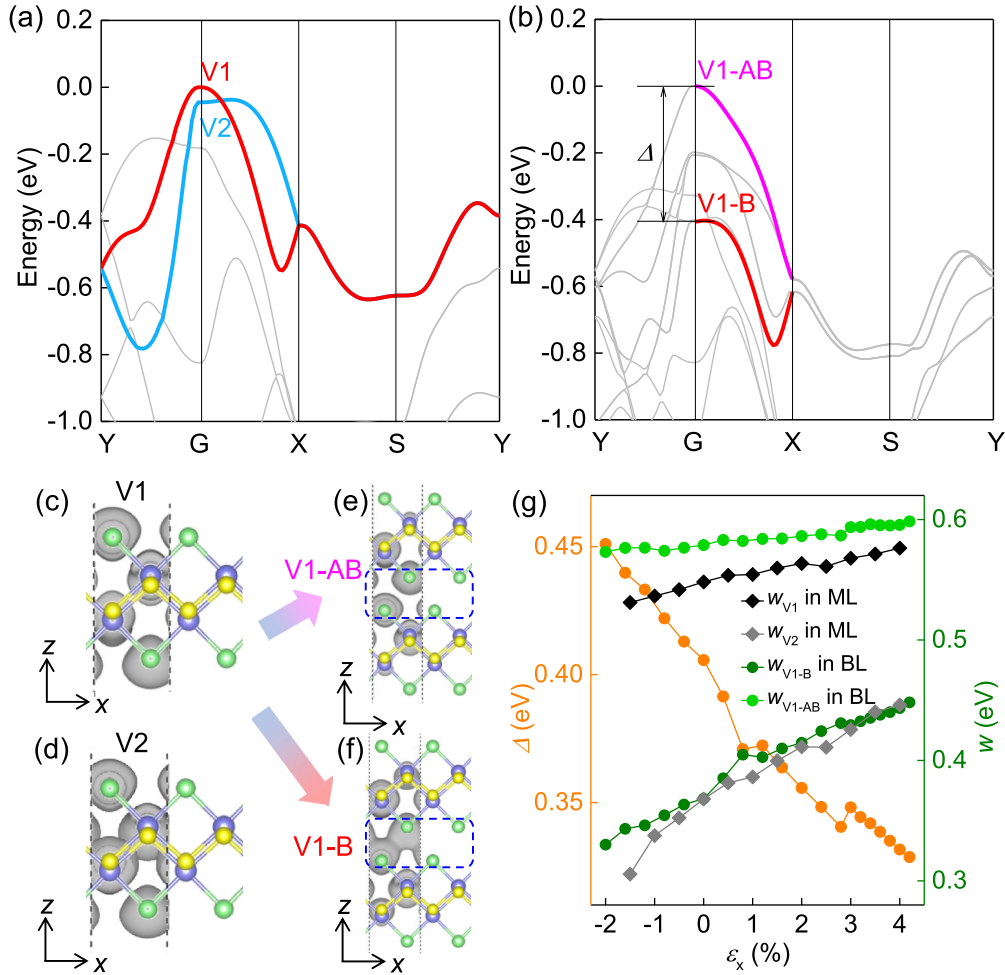


FIG. 3. Electronic band structures of strain-free monolayer (a) and bilayer (b) CrSBr. The two valence bands around the Fermi level in monolayer are labeled by V1 (red) and V2 (blue) in (a). For bilayer CrSBr, the interlayer bonding (V1-B) and antibonding (V1-AB) states of the V1 band marked in (a) were labeled by red and magenta lines, respectively, in (b). (c)–(f) Visualized squares of wavefunction norms for the labeled states in mono- and bilayer CrSBr with an isosurface value of  $3 \times 10^{-4}$  e/Bohr<sup>3</sup>. The interlayer antibonding and bonding regions were framed by blue dashed boxes. (g) Strain-dependent energy splitting between V1-B and V1-AB ( $\Delta$ ), bandwidths of V1 ( $w_{V1}$ ) and V2 ( $w_{V2}$ ) states in monolayer, and bonding ( $w_{V1-B}$ ) and antibonding ( $w_{V1-AB}$ ) states in bilayer along the  $G$ - $X$  direction.

the Br  $p_y$  components at the interlayer region [highlighted by blue dashed boxes in Figs. 3(e) and 3(f)]. The hybridization leads to an energy splitting ( $\Delta$ ) over 0.40 eV at the  $G$  point between the two original V1 states [Fig. 3(b)]. These two hybridized states are better illustrated using their wavefunctions [Fig. S6b (V1-AB) and S6c (V1-B)] and squares of wavefunction norms depicted in Fig. 3(e) (V1-AB) and Fig. 3(f) (V1-B).

The splitting energy  $\Delta$  reflects the strength of interlayer electronic hybridization and thus the degree of interlayer wave function overlapping. Under in-plane tensile strains along the  $x$  direction, the negative Poisson's ratio of the bilayer leads to enlarged interlayer spacing  $d$  [blue curve in Fig. 2(a)], which reduces the interlayer wave function overlapping and thus weakens the electronic hybridization. As a result, the energy splitting  $\Delta$  reduces from 0.45 eV at  $\varepsilon_x = -2.0\%$  to 0.33 eV at  $\varepsilon_x = 4.2\%$  [Fig. 3(g)]. The mechanism can also be obtained by density of states (DOS) analyses (Figs. S7a–S7d).

Although the  $x$  direction is stretched, the bandwidths are all enlarged in path  $G$ - $X$  for the original V1 band ( $w_{V1}$ ) of

the ML and the V1-B ( $w_{V1-B}$ ) and V1-AB ( $w_{V1-AB}$ ) bands of the BL [Fig. 3(g)]. The enlarged  $w_{V1}$  in the ML, without any interlayer interactions, indicates that the intralayer interaction, most likely, plays the primary role in bandwidth broadening. By comparison of the strained monolayers, we found that the stretched  $x$  lattice thins the monolayer (red squares in Fig. S8), promoting direct wavefunction overlaps of the V1 state along the  $x$  direction (see Fig. S9 for details). The promoted overlapping, resulting in increased  $w_{V1}$ , suggests that the  $x$  stretching gains additional kinetic energies to electrons moving within the layer, which is also validated in the strained bilayers. Both enlarged  $w_{V1-B}$  and  $w_{V1-AB}$  under  $x$  strain delocalize the interlayer sharing electrons along the  $x$  direction, consistent with the more delocalized interlayer DCDs plotted in Figs. 2(g)–2(j).

We next discuss the reasoning of the interlayer AFM-to-FM transition. The interlayer magnetism of layered magnets is usually determined by the competition between the interlayer Pauli repulsion energy and interlayer kinetic energy gain; the dominant term between the two energies



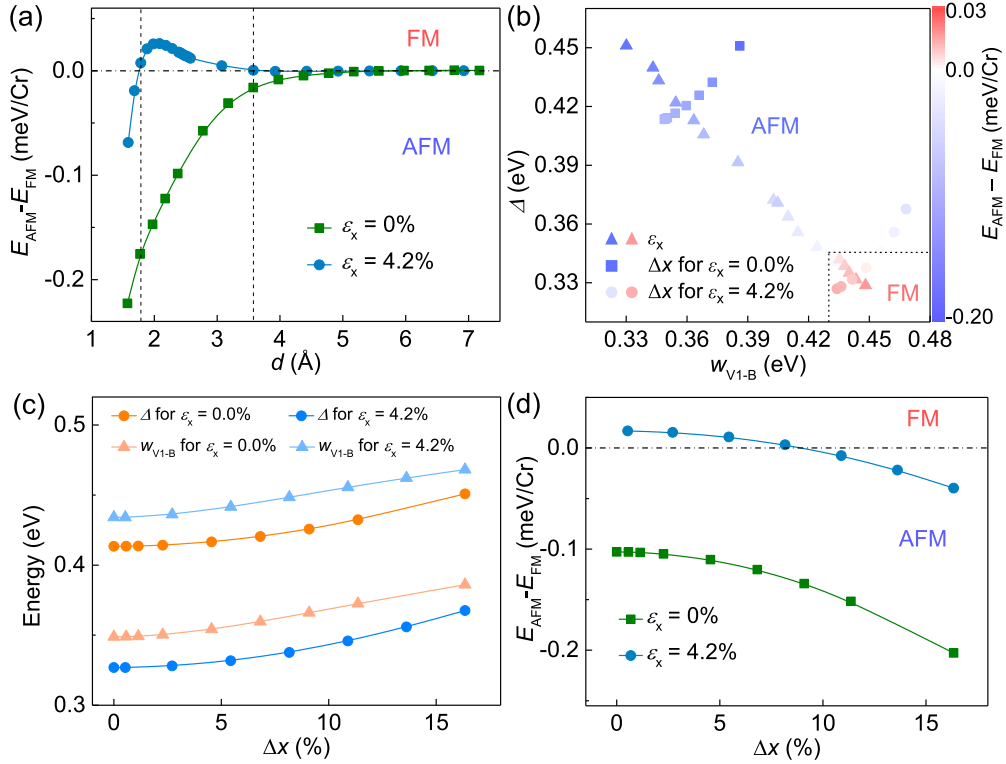


FIG. 4. Vertical and lateral sliding dependent-interlayer magnetic coupling. Energy difference between  $E_{\text{AFM}}$  and  $E_{\text{FM}}$  as functions of (a)  $d$  and (d) sliding along the  $x$  direction ( $\Delta x$ ) for  $\varepsilon_x = 0.0\%$  and  $4.2\%$ . The region within the vertical dashed lines in (a) represents interlayer FM coupling region. (b) A tentative phase diagram of the energy difference versus  $\Delta$  and  $w_{\text{V1-B}}$ . The black dashed box frames the interlayer FM region, where  $w_{\text{V1-B}}$  exceeds  $0.43$  eV and  $\Delta$  is less than  $0.34$  eV. (c)  $\Delta$  (circles) and  $w_{\text{V1-B}}$  (triangles) as a function of  $\Delta x$  for  $\varepsilon_x = 0.0\%$  and  $4.2\%$ , respectively.

varies as a function of the interlayer spacing [8]. A model Hamiltonian [8]  $H = -\sum_{i,j,\sigma=\downarrow,\uparrow} t_{ij}(C_{i\sigma}^\dagger C_{j\sigma} + \text{H.c.}) + \sum_i U_i n_{i\uparrow} n_{i\downarrow} + \sum_{\sigma=\downarrow,\uparrow} P_\sigma \rho_{or,\sigma}$  describes the interlayer interactions, in which the first and second terms are hopping and on-site Coulomb contributions across the vdW gap of the bilayer. The third term represents the Pauli repulsion at the overlapping region (OR) where  $\rho_{or,\sigma}$  denotes the electron density of the same spin component at the OR. It should be nearly zero if the bilayer is in the interlayer AFM configuration, but a positive value for the interlayer FM configuration. In the strong interlayer coupling regime, the Pauli repulsion is positively relevant to the overlapping and thus the energy splitting  $\Delta$ , while the kinetic energy is represented by bandwidth  $w$ . Thus, the larger (smaller) the  $\Delta$  ( $w$ ) value, the more favored the interlayer AFM configuration. However, the FM state could be largely promoted if this positive Pauli repulsion is sufficiently compensated by kinetic energy gains, namely smaller  $\Delta$  and larger  $w$ .

For  $\varepsilon_x = 0.0\%$ , the V1, V1-B, and V1-AB states are lesser delocalized [smaller  $w$ , Fig. 3(g)] such that the Pauli repulsion is dominated over the whole  $d$  range considered, i.e.,  $1.57$ – $7.17$  Å, which prefers the interlayer AFM configuration [green curve in Fig. 4(a)]. Under  $\varepsilon_x = 4.2\%$ , the further delocalization of these states [larger  $w$ , Fig. 3(g)] provides additional kinetic energy gains to transcend the Pauli repulsion. Thus, the interlayer FM state becomes more preferred [blue curve in Fig. 4(a)] for  $d$  values ranging  $1.79$ – $3.58$  Å [within the two vertical dashed lines in Fig. 4(a)], where the

Bethe-Slater-curve-like behavior [8] was reproduced. We also plotted a tentative phase diagram [Fig. 4(b)] for quantitatively describing the competitions as functions of  $w_{\text{V1-B}}$  and  $\Delta$ , which suggests that the interlayer FM state is, most likely, preferred when  $w_{\text{V1-B}}$  exceeds  $0.43$  eV and  $\Delta$  is less than  $0.34$  eV [black dashed box in Fig. 4(b)]. Therefore, the interlayer AFM state could transform to the FM state when decreasing hybridization splitting  $\Delta$  and broadening bandwidth  $w_{\text{V1-B}}$ , which could be achieved by increasing interlayer spacing and reducing layer thickness. We argue that interlayer sliding or element substitution also changes  $\Delta$  and/or  $w_{\text{V1-B}}$  in bilayer CrSBr, which may have a chance to induce this AFM-to-FM transition.

We used interlayer sliding to verify our model. Sliding along the  $x$  direction ( $\Delta x$ ) always enlarges either  $\Delta$  [circles in Fig. 4(c)] or  $w_{\text{V1-B}}$  [triangles in Fig. 4(c)]. Their relative values ( $w_{\text{V1-B}}/\Delta$ ), however, highly depend on the in-plane strain applied. At  $\varepsilon_x = 0.0\%$ , bandwidth  $w_{\text{V1-B}}$  is always smaller than hybridization splitting  $\Delta$  at any considered sliding distance [orange triangles versus orange circles in Fig. 4(c)]. In other words, the  $w_{\text{V1-B}}/\Delta$  ratio is always smaller than  $1.0$  ( $0.86$  in the present case). Thus, the dominant Pauli repulsion overwhelmingly favors the interlayer AFM coupling in the whole sliding range considered [green line in Fig. 4(d)]. The relative energies of  $w_{\text{V1-B}}$  and  $\Delta$  reverses ( $w_{\text{V1-B}} = 0.448$  eV and  $\Delta = 0.329$  eV) and the  $w_{\text{V1-B}}/\Delta$  ratio increases to  $1.36$  for  $\varepsilon_x = 4.2\%$ . This larger  $w_{\text{V1-B}}$  and smaller  $\Delta$  set favors the FM configuration at  $\Delta x = 0.0\%$ . As each layer of the bilayer

slides ( $\Delta x$  enlarges) to each other, the ratio, however, gradually drops to 1.32 ( $w_{V1-B} = 0.456$  eV and  $\Delta = 0.346$  eV) at  $\Delta x = 10.9\%$ , leading to an interlayer FM-to-AFM coupling transition [blue curve in Fig. 4(d)].

Substitution of interfacial Br with Cl atoms also modifies interlayer magnetism [37], ascribed to their different orbital radii and thus wavefunction overlaps. To isolate the effects of different orbital radii, we simply replaced Br atoms with Cl or I atoms, without further structural relaxations, in the strain-free CrSBr bilayer. As shown in Fig. S10, hybridization splitting  $\Delta$  (wave function overlapping) of the V1 states becomes more pronounced gradually from Cl ( $\Delta = 0.22$  eV) to I ( $\Delta = 0.84$  eV), ascribed to the largest orbital radius of I among Cl, Br, and I atoms. Moreover, the bandwidth of the V1-B state is 0.14 eV (0.47 eV) for CrSI (CrSCL), smaller (larger) than that for CrSBr (0.41 eV), which were also verified by plotting their interlayer DCDs in the real space (Fig. S11). As the atomic radius gradually increases from Cl to I, the overlapping among the  $p_y$  orbitals of the chalcogen atom strengthens and the bandwidth of the V1-B state narrows. These results further support our model that interlayer magnetism is tuned by intralayer electron delocalization and interlayer wavefunction overlapping in bilayer CrSX ( $X = \text{Cl/Br/I}$ ).

#### IV. CONCLUSIONS

In summary, we uncovered the mechanism of modulating interlayer magnetism using in-plane strains in CrSBr bilayer and few layers, in which the in-plane delocalization of electrons within a strained monolayer and the negative interlayer Poisson's ratio play paramount roles. We found that an in-plane tensile strain shrinks the layer thickness and pushes two Cr-S sublayers and two Br sublayers moving towards each other, which results in the enhanced overlapping of Cr  $d$ , S  $p$ , and Br  $p$  wavefunctions. As a result, the bandwidth of the highest valence band, reflecting in-plane electron delocalization, is enlarged 0.55–0.58 eV in the monolayer (0.37–0.45 eV for the bilayer) under an in-plane tensile strain of 4.2%. Another effect of the in-plane tensile strain lies in the resulting larger vdW gaps through a negative interlayer Poisson's ratio of  $-0.79$ , which reduces the interlayer wavefunction overlap

and thus the band splitting from 0.41 to 0.33 eV, significantly lowering the interlayer Pauli repulsion. The in-plane electron delocalization, together with the interlayer reduction of Pauli repulsion, causes the interlayer AFM-to-FM transition in the bilayer at 3.2% tensile  $x$  strain. This value is slightly larger than that reported in the experiment (1.4%) for CrSBr few layers [26], which is, at least partially, because of a thicker layer measured in the experiment. The thicker layer usually has a larger cross-layer kinetic energy than the bilayer [32], resulting in the transition occurring at a smaller strain value (Fig. S12a). In addition, the transition is accompanied by a piezomagnetic effect where piezomagnetic coefficient  $d_{12}$  under the 3.2% strain was theoretically derived to be  $1.29 \mu\text{g/kbar}$ . This value is comparable to those of other piezomagnetic materials, such as  $1.92 \mu\text{g/kbar}$  of  $\text{Mn}_3\text{Ga}_{0.95}\text{N}_{0.94}$  [38] and  $4.27 \mu\text{g/kbar}$  for  $\text{Mn}_{0.87}\text{Fe}_{0.13}\text{NiGe}$  [39]. An alternative way to tune the interlayer AFM-FM transition of CrSBr is to apply magnetic fields, which induce the nucleation and subsequent propagation of an AFM-FM phase wall [40] and anisotropic optical reflectivity [41]. The feasible in-plane strain tuned interlayer AFM-FM transition provides a unique category of methods to manipulate interlayer magnetism, differently from those known ones by applying interlayer modulations like out-of-plane strain [8], sliding [13,14], doping [18], and changing number of layers [11].

#### ACKNOWLEDGMENTS

We gratefully acknowledge financial support from the Ministry of Science and Technology (MOST) of China (Grants No. 2023YFA1406500 and No. 2018YFE0202700), the National Natural Science Foundation of China (Grants No. 11974422, No. 12204534, and No. 12104504), the Strategic Priority Research Program of Chinese Academy of Sciences (Grant No. XDB30000000), the Fundamental Research Funds for the Central Universities, and the Research Funds of Renmin University of China (Grant No. 22XNKJ30). N.L. was supported by the China Postdoctoral Science Foundation (Grant No. 2022M713447). All calculations for this study were performed at the Physics Lab of High-Performance Computing (PLHPC) and the Public Computing Cloud (PCC) of Renmin University of China.

- 
- [1] J. F. Dobson and T. Gould, Calculation of dispersion energies, *J. Phys.: Condens. Matter* **24**, 073201 (2012).
  - [2] Z.-X. Hu, X. Kong, J. Qiao, B. Normand, and W. Ji, Interlayer electronic hybridization leads to exceptional thickness-dependent vibrational properties in few-layer black phosphorus, *Nanoscale* **8**, 2740 (2016).
  - [3] Y. Zhao, J. Qiao, P. Yu, Z. Hu, Z. Lin, S. P. Lau, Z. Liu, W. Ji, and Y. Chai, Extraordinarily strong interlayer interaction in 2D layered  $\text{PtS}_2$ , *Adv. Mater.* **28**, 2399 (2016).
  - [4] J. Xia, J. Yan, Z. Wang, Y. He, Y. Gong, W. Chen, T. C. Sum, Z. Liu, P. M. Ajayan, and Z. Shen, Strong coupling and pressure engineering in  $\text{WSe}_2$ - $\text{MoSe}_2$  heterobilayers, *Nat. Phys.* **17**, 92 (2021).
  - [5] N. Peimyo, T. Deilmann, F. Withers, J. Escolar, D. Nutting, T. Taniguchi, K. Watanabe, A. Taghizadeh, M. F. Craciun, and K. S. Thygesen, Electrical tuning of optically active interlayer excitons in bilayer  $\text{MoS}_2$ , *Nat. Nanotechnol.* **16**, 888 (2021).
  - [6] J. Qiao, X. Kong, Z.-X. Hu, F. Yang, and W. Ji, High-mobility transport anisotropy and linear dichroism in few-layer black phosphorus, *Nat. Commun.* **5**, 4475 (2014).
  - [7] L. Sheng, G. Tai, Y. Yin, C. Hou, and Z. Wu, Layer-dependent exciton modulation characteristics of 2D  $\text{MoS}_2$  driven by acoustic waves, *Adv. Opt. Mater.* **9**, 2001349 (2021).
  - [8] C. Wang, X. Zhou, L. Zhou, Y. Pan, Z.-Y. Lu, X. Wan, X. Wang, and W. Ji, Bethe-Slater-curve-like behavior and interlayer spin-exchange coupling mechanisms in two-dimensional magnetic bilayers, *Phys. Rev. B* **102**, 020402(R) (2020).
  - [9] Z. Sun, Y. Yi, T. Song, G. Clark, B. Huang, Y. Shan, S. Wu, D. Huang, C. Gao, Z. Chen, M. McGuire, T. Cao, D. Xiao, W.-T. Liu, W. Yao, X. Xu, and S. Wu, Giant nonreciprocal

- second-harmonic generation from antiferromagnetic bilayer CrI<sub>3</sub>, *Nature (London)* **572**, 497 (2019).
- [10] B. Huang, G. Clark, E. Navarro-Moratalla, D. R. Klein, R. Cheng, K. L. Seyler, D. Zhong, E. Schmidgall, M. A. McGuire, D. H. Cobden, W. Yao, D. Xiao, P. Jarillo-Herrero, and X. Xu, Layer-dependent ferromagnetism in a van der Waals crystal down to the monolayer limit, *Nature (London)* **546**, 270 (2017).
- [11] C. Gong, L. Li, Z. Li, H. Ji, A. Stern, Y. Xia, T. Cao, W. Bao, C. Wang, and Y. Wang, Discovery of intrinsic ferromagnetism in two-dimensional van der Waals crystals, *Nature (London)* **546**, 265 (2017).
- [12] T. Li, S. Jiang, N. Sivadas, Z. Wang, Y. Xu, D. Weber, J. E. Goldberger, K. Watanabe, T. Taniguchi, C. J. Fennie, K. Fai Mak, and J. Shan, Pressure-controlled interlayer magnetism in atomically thin CrI<sub>3</sub>, *Nat. Mater.* **18**, 1303 (2019).
- [13] P. Jiang, C. Wang, D. Chen, Z. Zhong, Z. Yuan, Z.-Y. Lu, and W. Ji, Stacking tunable interlayer magnetism in bilayer CrI<sub>3</sub>, *Phys. Rev. B* **99**, 144401 (2019).
- [14] T. Song, Z. Fei, M. Yankowitz, Z. Lin, Q. Jiang, K. Hwangbo, Q. Zhang, B. Sun, T. Taniguchi, K. Watanabe, M. A. McGuire, D. Graf, T. Cao, J.-H. Chu, D. H. Cobden, C. R. Dean, D. Xiao, and X. Xu, Switching 2D magnetic states via pressure tuning of layer stacking, *Nat. Mater.* **18**, 1298 (2019).
- [15] B. Huang, G. Clark, D. R. Klein, D. MacNeill, E. Navarro-Moratalla, K. L. Seyler, N. Wilson, M. A. McGuire, D. H. Cobden, D. Xiao, W. Yao, P. Jarillo-Herrero, and X. Xu, Electrical control of 2D magnetism in bilayer CrI<sub>3</sub>, *Nat. Nanotechnol.* **13**, 544 (2018).
- [16] E. S. Morell, A. León, R. H. Miwa, and P. Vargas, Control of magnetism in bilayer CrI<sub>3</sub> by an external electric field, *2D Mater.* **6**, 025020 (2019).
- [17] N. Liu, S. Zhou, and J. Zhao, High-Curie-temperature ferromagnetism in bilayer CrI<sub>3</sub> on bulk semiconducting substrates, *Phys. Rev. Mater.* **4**, 094003 (2020).
- [18] C. Wang, X. Zhou, Y. Pan, J. Qiao, X. Kong, C.-C. Kaun, and W. Ji, Layer and doping tunable ferromagnetic order in two-dimensional CrS<sub>2</sub> layers, *Phys. Rev. B* **97**, 245409 (2018).
- [19] Y. Guo, N. Liu, Y. Zhao, X. Jiang, S. Zhou, and J. Zhao, Enhanced ferromagnetism of CrI<sub>3</sub> bilayer by self-intercalation, *Chin. Phys. Lett.* **37**, 107506 (2020).
- [20] Y. Xu, A. Ray, Y.-T. Shao, S. Jiang, K. Lee, D. Weber, J. E. Goldberger, K. Watanabe, T. Taniguchi, D. A. Muller, K. F. Mak, and J. Shan, Coexisting ferromagnetic–antiferromagnetic state in twisted bilayer CrI<sub>3</sub>, *Nat. Nanotechnol.* **17**, 143 (2022).
- [21] H. Yu, J. Zhao, and F. Zheng, Interlayer magnetic interactions in  $\pi/3$ -twisted bilayer CrI<sub>3</sub>, *Appl. Phys. Lett.* **119**, 222403 (2021).
- [22] L. Wu, L. Zhou, X. Zhou, C. Wang, and W. Ji, In-plane epitaxy-strain-tuning intralayer and interlayer magnetic coupling in CrSe<sub>2</sub> and CrTe<sub>2</sub> monolayers and bilayers, *Phys. Rev. B* **106**, L081401 (2022).
- [23] L. Webster and J.-A. Yan, Strain-tunable magnetic anisotropy in monolayer CrCl<sub>3</sub>, CrBr<sub>3</sub>, and CrI<sub>3</sub>, *Phys. Rev. B* **98**, 144411 (2018).
- [24] Z. Wu, J. Yu, and S. Yuan, Strain-tunable magnetic and electronic properties of monolayer CrI<sub>3</sub>, *Phys. Chem. Chem. Phys.* **21**, 7750 (2019).
- [25] K. Chen, X. Yan, J. Deng, C. Bo, M. Song, D. Kan, J. He, W. Huo, and J. Z. Liu, Out-of-plane pressure and electron doping inducing phase and magnetic transitions in GeC/CrS<sub>2</sub>/GeC van der Waals heterostructure, *Nanoscale* **16**, 3693 (2024).
- [26] J. Cenker, S. Sivakumar, K. Xie, A. Miller, P. Thijssen, Z. Liu, A. Dismukes, J. Fonseca, E. Anderson, X. Zhu, X. Roy, D. Xiao, J.-H. Chu, T. Cao, and X. Xu, Reversible strain-induced magnetic phase transition in a van der Waals magnet, *Nat. Nanotechnol.* **17**, 256 (2022).
- [27] E. J. Telford, A. H. Dismukes, K. Lee, M. Cheng, A. Wieteska, A. K. Bartholomew, Y.-S. Chen, X. Xu, A. N. Pasupathy, X. Zhu, C. R. Dean, and X. Roy, Layered antiferromagnetism induces large negative magnetoresistance in the van der Waals semiconductor CrSBr, *Adv. Mater.* **32**, 2003240 (2020).
- [28] J. P. Perdew, K. Burke, and M. Ernzerhof, Generalized gradient approximation made simple, *Phys. Rev. Lett.* **77**, 3865 (1996).
- [29] G. Kresse and D. Joubert, From ultrasoft pseudopotentials to the projector augmented-wave method, *Phys. Rev. B* **59**, 1758 (1999).
- [30] See Supplemental Material at <http://link.aps.org/supplemental/10.1103/PhysRevB.109.214422> for on-site Coulomb  $U$  test of magnetism of bilayer CrSBr, magnetic configurations in calculating exchange parameters, effects of epitaxial strains and a uniaxial strain along the  $y$  direction, strain-dependent charge variations across the Cr atoms of interlayer differential charge densities, electron localization function (ELF), squares of wavefunction norms of the labeled states in Figs. 3(a) and 3(b), density of states at the Gamma point for bilayer CrSBr under uniaxial  $x$ -strains, layer thickness, squares of wavefunction norms of the V1 state for monolayer CrSBr under  $\varepsilon_x = 0.0\%$  and  $\varepsilon_x = 4.0\%$ , and effects of Cl and I substitution.
- [31] C. Ye, C. Wang, Q. Wu, S. Liu, J. Zhou, G. Wang, A. Söll, Z. Sofer, M. Yue, X. Liu, M. Tian, Q. Xiong, W. Ji, and X. Renshaw Wang, Layer-dependent interlayer antiferromagnetic spin reorientation in air-stable semiconductor CrSBr, *ACS Nano* **16**, 11876 (2022).
- [32] B. Li, Z. Wan, C. Wang, P. Chen, B. Huang, X. Cheng, Q. Qian, J. Li, Z. Zhang, G. Sun, B. Zhao, H. Ma, R. Wu, Z. Wei, Y. Liu, L. Liao, Y. Ye, Y. Huang, X. Xu, X. Duan, W. Ji, and X. Duan, Van der Waals epitaxial growth of air-stable CrSe<sub>2</sub> nanosheets with thickness-tunable magnetic order, *Nat. Mater.* **20**, 818 (2021).
- [33] S. Lu, D. Guo, Z. Cheng, Y. Guo, C. Wang, J. Deng, Y. Bai, C. Tian, L. Zhou, Y. Shi, J. He, W. Ji, and C. Zhang, Controllable dimensionality conversion between 1D and 2D CrCl<sub>3</sub> magnetic nanostructures, *Nat. Commun.* **14**, 2465 (2023).
- [34] Y. Wang, N. Luo, J. Zeng, L.-M. Tang, and K.-Q. Chen, Magnetic anisotropy and electric field induced magnetic phase transition in the van der Waals antiferromagnet CrSBr, *Phys. Rev. B* **108**, 054401 (2023).
- [35] K. Yang, G. Wang, L. Liu, D. Lu, and H. Wu, Triaxial magnetic anisotropy in the two-dimensional ferromagnetic semiconductor CrSBr, *Phys. Rev. B* **104**, 144416 (2021).
- [36] C. Wang, X. Zhou, L. Zhou, N.-H. Tong, Z.-Y. Lu, and W. Ji, A family of high-temperature ferromagnetic monolayers with locked spin-dichroism-mobility anisotropy: MnNX and CrCX ( $X = \text{Cl, Br, I}$ ;  $C = \text{S, Se, Te}$ ), *Sci. Bull.* **64**, 293 (2019).
- [37] E. J. Telford, D. G. Chica, M. E. Ziebel, K. Xie, N. S. Manganaro, C.-Y. Huang, J. Cox, A. H. Dismukes, X. Zhu, J. P. S. Walsh, T. Cao, C. R. Dean, and X. Roy, Designing magnetic properties in CrSBr through hydrostatic pressure and ligand substitution, *Adv. Phys. Res.* **2**, 2300036 (2023).
- [38] K. Shi, Y. Sun, J. Yan, S. Deng, L. Wang, H. Wu, P. Hu, H. Lu, M. I. Malik, Q. Huang, and C. Wang, Baromagnetic effect

- in antiperovskite  $\text{Mn}_3\text{Ga}_{0.95}\text{N}_{0.94}$  by neutron powder diffraction analysis, *Adv. Mater.* **28**, 3761 (2016).
- [39] F. Shen, H. Zhou, F. Hu, J.-T. Wang, H. Wu, Q. Huang, J. Hao, Z. Yu, Y. Gao, Y. Lin, Y. Wang, C. Zhang, Z. Yin, J. Wang, S. Deng, J. Chen, L. He, T. Liang, J.-R. Sun, T. Zhao, and B. Shen, A distinct spin structure and giant baromagnetic effect in MnNiGe compounds with Fe-Doping, *J. Am. Chem. Soc.* **143**, 6798 (2021).
- [40] M. A. Tschudin, D. A. Broadway, P. Reiser, C. Schrader, E. J. Telford, B. Gross, J. Cox, A. E. Dubois, D. G. Chica, and R. Rama-Eiroa, Nanoscale magnetism and magnetic phase transitions in atomically thin CrSBr, [arXiv:2312.09279](https://arxiv.org/abs/2312.09279).
- [41] J. Yu, D. Liu, Z. Ding, Y. Yuan, J. Zhou, F. Pei, H. Pan, T. Ma, F. Jin, and L. Wang, Direct imaging of antiferromagnet-ferromagnet phase transition in van der Waals antiferromagnet CrSBr, *Adv. Funct. Mater.* **34**, 2307259 (2024).